Research Article

ADVANCED PHOTONICS

Unconventional bound states in the continuum from metamaterial-induced electron acoustic waves

Wenhui Wang[a,*] Antonio Günzler,[a] Bodo D. Wilts[a,b] Ullrich Steiner,[a] and Matthias Saba[a,*]
[a]University of Fribourg, Adolphe Merkle Institute, Fribourg, Switzerland
[b]University of Salzburg, Department of Chemistry and Physics of Materials, Salzburg, Austria

Abstract. Photonic bound states in the continuum (BICs) are spatially localized modes with infinitely long lifetimes, which exist within a radiation continuum at discrete energy levels. These states have been explored in various systems, including photonic and phononic crystal slabs, metasurfaces, waveguides, and integrated circuits. Robustness and availability of the BICs are important aspects for fully taming the BICs toward practical applications. Here, we propose a generic mechanism to realize BICs that exist by first principles free of fine parameter tuning based on non-Maxwellian double-net metamaterials (DNMs). An ideal warm hydrodynamic double plasma (HDP) fluid model provides a homogenized description of DNMs and explains the robustness of the BICs found herein. In the HDP model, these are standing wave formations made of electron acoustic waves (EAWs), which are pure charge oscillations with vanishing electromagnetic fields. EAW BICs have various advantages, such as (i) frequency-comb-like collection of BICs free from normal resonances; (ii) robustness to symmetry-breaking perturbations and formation of quasi-BICs with an ultrahigh Q-factor even if subject to disorder; and (iii) giving rise to subwavelength microcavity resonators hosting quasi-BIC modes with an ultrahigh Q-factor.

Keywords: bound states in the continuum; double-net metamaterial; metamaterial; electron acoustic wave; hydrodynamical plasma.

Received Mar. 28, 2023; revised manuscript received Jul. 1, 2023; accepted for publication Aug. 4, 2023; published online Sep. 4, 2023.

[DOI: 10.1117/1.AP.5.5.056005]

1 Introduction

As early as 1929, von Neumann and Wigner constructed spatially localized bound states in the continuum (BICs) as solutions of the single particle Schrödinger equation with energies above the associated potential.[1,2] BICs are, however, general wave phenomenona and are therefore not restricted to quantum mechanics and have recently been demonstrated in a variety of classical wave systems.[3–14] Among these different demonstrations, light–matter interactions endowed by BICs in periodic systems have recently gained strong attention and have been exploited for applications in biosensing,[15,16] vortex beam generation,[17,18] high-Q resonators, and lasing.[9,19–22] To date, several mechanisms for generating BICs in the periodic systems have been reported, including (i) symmetry-guaranteed mode mismatching, (ii) destructive interference with a topological origin,[3] and (iii) the Friedrich–Wintgen mechanism.[23–25] Recent evidence, however, suggests that currently available BICs provide unreliable lifetimes. For example, mechanism (i) yields BICs that are readily destroyed by small symmetry-breaking perturbations[20,26,27] and couple to higher diffraction orders.[28] Such features lead to quasi-BIC states with manageable lifetimes. On the other hand, mechanism (ii) gives rise to BICs that are easily shifted in momentum space (excitation angle). Furthermore, non-BIC modes typically exist spectrally close to these BICs,[4] which cannot easily be eliminated through existing design principles. BICs created by mechanism (iii) are, for example, realized by the destructive interference between two optical modes satisfying the Friedrich–Wintgen condition

*Address all correspondence to Wenhui Wang, rainbowwh6@gmail.com; Matthias Saba, matthias.saba@unifr.ch

and are, therefore, always accompanied by a constructive interference background mode.

Heuristically, an alternative approach to generating photonic BICs is to engineer a material that supports a pure charge wave with a vanishing electromagnetic (EM) field. While such a wave cannot exist in all-dielectric materials, it is naturally obtained in a non-Maxwellian hydrodynamic double plasma (HDP). We show that such an HDP can be approximately realized through double-net metamaterials (DNMs). Metamaterials are artificial structures, typically made of periodically arranged elements, so-called meta-atoms, on a lattice significantly smaller than the wavelength of interest.[29] These structures locally mimic the quasi-homogeneous light–matter interaction of ordinary materials but give access to optical properties that cannot be found in nature, including negative refraction,[30,31] near-zero refractive index,[32,33] and strong chiro-optical effects.[34–36] Fully connected metallic network-like metamaterials mimic the EM response of bulk metals. In contrast to bulk metals, whose plasma frequency is typically in the ultraviolet, the effective plasma frequency of metallic network-like metamaterials can be tuned to a specific wavelength range of interest.[37,38] Network metamaterials can be manufactured for visible wavelength operation via self-assembly, where they have been associated with several interesting effects, such as linear and circular dichroism.[36,39,40] DNMs, also referred to as interlaced wire media, consist of two intertwining, spatially separated metallic network domains and offer the generation of a fundamentally new physics. DNMs have only recently gained theoretical interest in the context of negative index ellipsoids,[41] a light tunneling anomaly,[42] and longitudinal mode propagation.[43] An experimental realization of an optical gyroid DNM dates back to 2011,[44] while a microwave DNM has been reported recently.[45]

Here, we propose a generic effective medium approach to generate a new type of HDP photonic BICs in DNMs. In contrast to existing designs, the proposed BICs are formed by pure charge fluctuations with a vanishing EM field, also known as electron acoustic wave (EAW) in HDPs. These BICs are spectrally isolated from normal resonances, robust against a large class of perturbations. Most surprisingly, they retain an ultrahigh Q-factor within a subwavelength DNM microcavity resonator, even below the diffraction limit. They exist within a broad spectral range, free of non-BIC resonances and their frequency spacing can be freely tuned by the size of the structure, reaching spectrally dense BICs for an optically thick DNM slab in the absence of non-BIC modes.

2 Electronic Acoustic Wave in Double-Net Metamaterials

To better understand the formation of the new type of BIC modes in DNMs, we first derive and discuss the nature of the bulk states, particularly the new EAWs, in the context of metamaterials. We start with the HDP model. The HDP is formally described by (i) particle conservation to describe the individual charge carrier dynamics; (ii) the hydrodynamic Navier–Stokes equations and the Lorentz force to model particle–particle and light–particle interactions; and (iii) the Maxwell equations, which describe the light-field dynamics. A detailed derivation of the HDP model can be found in Note S1 in the Supplementary Material.

For convenience, we restrict the discussion to a nondissipative model and therefore, to low frequencies, where the constituting metals are well approximated by a perfect electric conductor. We further introduce the plasma frequency $\omega_{pi} := \sqrt{n_{0i} q_i^2 / m_i}$ and the nondimensional thermal pressure parameter $\kappa_i := \sqrt{\gamma p_i / (n_{0i} m_i c^2)}$ for the two charge carriers labeled $i = 1, 2$, which remain the only free parameters in the model. These two parameters depend on the equilibrium charge carrier density n_{0i}, the charge q_i, the effective mass m_i, the equilibrium pressure p_i, the adiabatic exponent γ, and the speed of light in vacuum c. Through a plane-wave approach and by linearizing the HDP model,[46,47] the generally complex problem is transformed into a 14-dimensional linear eigenproblem for the eigenfrequency ω (see Note S1 in the Supplementary Material for a detailed derivation). The components of the eigenvector in this low-dimensional problem with eigenfrequency ω are the electric and magnetic field amplitudes $\mathbf{E}$ and $\mathbf{H}$ and the amplitude of the charge carrier density fluctuations δn_i and the corresponding current density $\mathbf{j}_i$ for each plasma (labeled $i = 1, 2$).

The band structure of the linearized HDP, obtained by solving the eigenvalue problem, is shown on the left in Fig. 1(b) (note that we only show the physically relevant positive frequencies). From high to low frequencies, we obtain the two-fold degenerate EM transverse band (EMW) (cyan), the longitudinal Langmuir band (LMW) (black), both of which are hyperbolic, emerging from $\omega = (\omega_{p1}^2 + \omega_{p2}^2)^{1/2}$ for wavenumber $k = 0$, and the linear EAW band emanating from $\omega = 0$. The application of $k \cdot p$ theory[48] to the Γ-point to construct an effective Hamiltonian for the EAW band predicts a slope of $\omega_a^2 = (m^2 + \frac{\kappa_2^2}{\kappa_1^2}) \frac{1}{m^2+1} \kappa_1^2 c^2 k_a^2$, where $m = \frac{\omega_{p1}}{\omega_{p2}}$ (Note S1.3 in the Supplementary Material). This reduces to the approximated form $\omega_a = c\kappa_1 k_a$ for equal plasma parameters. For equal pressure parameters $\kappa_1 = \kappa_2$, the EAW modes consist of oppositely drifting charge waves with $\delta n_1 = -\delta n_2$ and $\mathbf{j}_1 = -\mathbf{j}_2 \| \mathbf{k}$ and vanishing EM fields $\mathbf{E} = \mathbf{H} = 0$ [Fig. 1(a)]. Due to this zero EM nature and the resulting decoupling from the EM vacuum modes, the EAW naturally forms BICs in the presence of a photonic radiation continuum. In a natural HDP, the two charge carrier species of the plasma, usually two frictionless electrons and ions, interact so that the model described above only applies in a limit, and extremely strict conditions are necessary to construct an observable EAW system.[49] Even though the EAW may play an important role in space physics, due to broadband electrostatic noise observed in the Earth's auroral region, there has been little experimental work on this mode in the laboratory.[50–52]

Concurrently, single 3D metallic network metamaterials (Note S1.2 in the Supplementary Material) have been shown to act as an effective realization of a single species plasma with ultralow effective plasma frequency in the gigahertz range.[53] An effective hydrodynamic behavior beyond the standard constitutive equations that leads to a nonlocal response can be understood through a charge accumulation and release effect.[37,38] To circumvent the difficulties in creating a natural double-plasma,[49–51] we employ a DNM lattice, whose fully connected wire morphology effectively provides a freely moving double-plasma with finite equilibrium charge carrier density and Coulomb pressure, leading to a behavior that resembles a plasma with an exact electronic thermal pressure. The double-plasma [Eq. (S14) in the Supplementary Material] and the plasmonic network

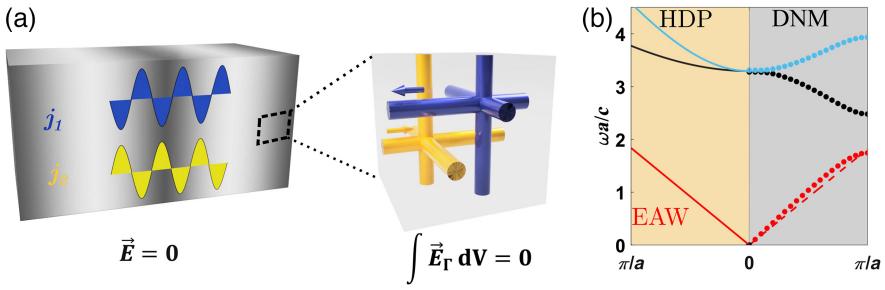

Fig. 1 (a) Schematic diagram of the EAW mode in the HDP fluid. Blue and yellow curves represent the two counterpropagating charge carriers, resulting in a vanishing field. DNMs consist of two interwoven percolating metallic nets supporting the two opposing currents, analogous to the two counterpropagating carriers in the HDP. In the electrostatic limit, DNMs are equivalent to HDPs, with a homogenized EM field that vanishes at the Γ point. (b) Dispersion relation of an HDP with $\kappa_{1,2} = \frac{1}{\sqrt{3}}$, featuring a light-like EM wave (EMW) (cyan solid line), a longitudinal Langmuir wave (LMW) (solid black line), and the EAW (solid red line). The corresponding band structure of the unperturbed DNM is shown on the right, illustrating that the three modes resemble those of the HDP. The slope of the fundamental band (dashed red line) is in good agreement with the HDP theoretical model.

eigenproblem [Eq. (S20) in the Supplementary Material] are indeed formally identical, as we have shown in Note S1 in the Supplementary Material. Note that the effective thermal pressures are mainly determined by the connectivity of the wires, leading to $\kappa_{1,2} \approx \frac{1}{\sqrt{3}}$, due to the vertically intersecting morphology in the three axes. For finite radii, $\kappa_{1,2}$ are adjusted through the radius of the networks,[54] giving more accurate values of the EAW band's slope (see Note S1.4 in the Supplementary Material for details and Note S3 in the Supplementary Material for an illustration of this effect). In practice, the wire-mesh pressure parameter falls in a range between $\kappa \approx 2/3$ for a wire radius of $r = a/100$ and $\kappa \approx 3/4$ for $r = a/5$. A quasi-static circuitry theory of multinet metamaterials has been proposed to predict the low-frequency dispersion,[55] but not the EAW nature. The DNM structures discussed in this paper are composed of two single nets of fully connected metal cylinders along the cubic axes with radii $r_{1,2}$, which may differ between the two nets. We use the notation $\mathbf{P} := (r_1, r_2, d)$ to represent the network parameters. d is the offset of the two networks that are shifted by $\mathbf{S} = (1,1,1)^\intercal d$. The double network with $d = \frac{a}{2}$ is the pcu-c net with $\mathrm{Im}\bar{3}m$ symmetry. Throughout this paper, the lattice constant is $a = 5$ mm.

The numerically simulated band structure of a DNM with $\mathbf{P} = (0.4, 0.4, \frac{a}{3})$ is illustrated in Fig. 1(b) and features a fundamental band with linear slope (red dotted line) that emanates from the Γ-point at zero frequency. This result not only qualitatively matches the EAW band in the HDP model, but the dispersion is indeed in good agreement with the approximation from Note S1 in the Supplementary Material in the limit of thin wires $\omega = \frac{1}{\sqrt{3}} ck$ (red dashed line). As expected from the HDP model, this slope mainly depends on κ and only weakly depends on the quotient of the effective plasma frequencies. Our theory is valid within a large variety of parameters of DNMs, confirmed by numerical simulations for various values of $\mathbf{P}$ (Note S2 and Fig. S3 in the Supplementary Material). For larger wave vectors closer to the boundary of the Brillouin zone, the long wavelength limit breaks down, and the slope deviates and becomes zero at the X-point [$\mathbf{k} = (\pi/a, 0, 0)$] due to time-reversal symmetry.[48] Analogously to the EAW in the HDP model, the two networks in the DNM carry opposing currents, indicated by arrows in Fig. 1(a). The simulated surface current densities $\mathbf{J}$ for DNMs with equivalent radii and different offsets [$\mathbf{P} = (0.4, 0.4, \frac{a}{3})$ and $\mathbf{P} = (0.4, 0.4, \frac{a}{2})$] are shown in Fig. 2(a). They indeed exhibit almost exactly opposite J_x in the two networks at a small k ($k_x = 0.05\pi/a$ and $k_{y,z} = 0$). For different radii [$\mathbf{P} = (0.4, 0.1, \frac{a}{3})$], a weaker current density is observed on the larger radius network, whose integrated magnitude equals the opposing current density of the lower-radius network. This implies that the total current remains zero, irrespective of the network radii, consistent with the HDP model.

To investigate the microscopic EM fields of the EAW-like modes in DNMs, we compute their unit-cell-averaged electric field components of the fundamental mode, normalized by the averaged electric field intensity. The averaged transverse components vanish over the entire Brillouin zone (Figs. S4 and S5 in the Supplementary Material), while the longitudinal component quadratically increases with the length of the wave vector [Fig. 2(a)]. Therefore, the fundamental modes in DNMs are quasi-longitudinal with $\mathbf{E} \| \mathbf{k}$. We conclude that the HDP model is a valid effective medium description for DNMs in the static limit. DNMs provide a metamaterial realization of HDPs, which require extremely stringent restrictions in natural plasmas for their laboratory observation. We finally note that the notion of an effective permittivity seems misleading due to the non-Maxwellian nature of the EAW mode, meaning the lack of EM fields. In this context, a previously reported homogenization approach[56] leading to an effective permittivity ε_h for the DNM only accurately describes the Langmuir mode residing above the effective plasma frequencies. In contrast with standard metamaterial homogenization approaches, the HDP model developed here yields a fully consistent, effective medium description of the fundamental DNM band and accurately predicts both the phase velocity and the associated fields. Even though the discussion in this paper is restricted to Cartesian wire meshes as shown Fig. 1, we show that the HDP model applies equally

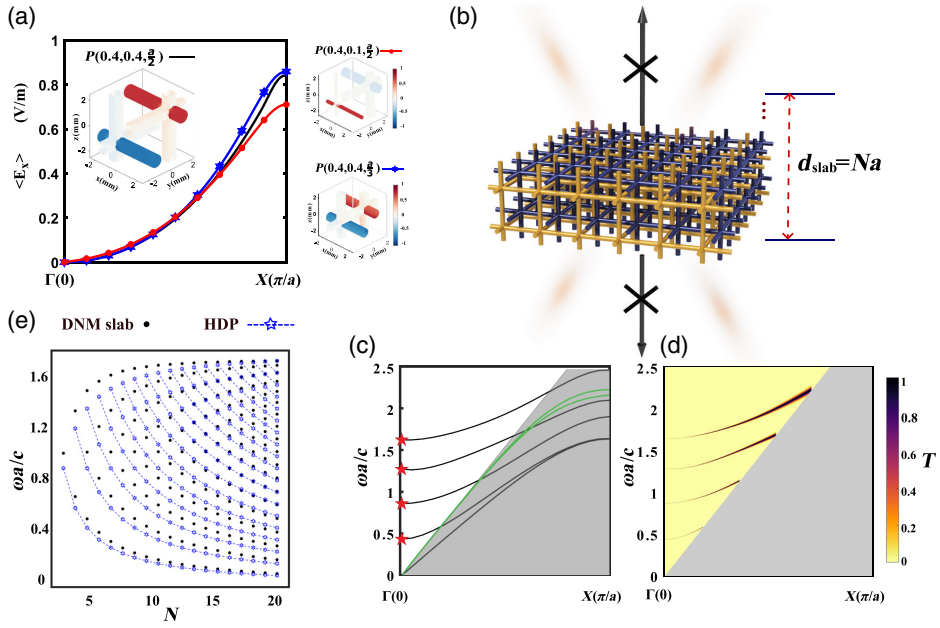

Fig. 2 (a) Magnitude of the electric field for the homogenized longitudinal EAW band components along the $\Gamma - X$ direction. The three curves correspond to DNMs with paramter sets of $\mathbf{P} = (0.4, 0.4, \frac{a}{2})$ (black line), $\mathbf{P} = (0.4, 0.4, \frac{a}{3})$ (blue line), and $\mathbf{P} = (0.4, 0.1, \frac{a}{2})$ (red line). (b) Schematic diagram of a DNM slab with finite thickness embedded in a vacuum. The BICs on the Γ point are decoupled from vacuum radiation and only weakly couple when the wave vector deviates from the Γ-point. (c) In-plane bandstructure of a DNM with $\mathbf{P} = (0.4, 0.4, \frac{a}{2})$ slab. The DNM slab extends over $N = 5$ unit cells in z-direction. The solid black lines are quasi-BIC states of EAW modes that weakly couple to vacuum radiation above the light line. The first black solid line below the light line is made of an in-plane EAW wave and therefore resembles the bulk dispersion, while the upper four black solid lines correspond to EAW standing waves. BICs exist at the Γ-point and are marked by red pentagrams. The two cyan lines are spoof plasmon surface modes. The region outside of the light cone is shaded in gray. (d) Corresponding heatmap of the transmissivity for an incoming plane wave from one side of the slab within the light cone. The reflectivity is 1, except close to the EAW standing wave bands, which leads to a Fabry–Pérot-like behavior with a high Q-factor that rapidly reaches infinity at the Γ-point. (e) Frequency of the BIC modes at the Γ-point as a function of the number of unit cells N in the DNM slab in z-direction. The black dots are calculated by full-wave simulations, and the blue points, connected by a dashed line that serves as a guide to the eye, are from the HDP model under hard wall boundary conditions.

to other DNM geometries in Note S3 in the Supplementary Material (Figs. S4 and S5 in the Supplementary Material).

3 Bound States in the Continuum in Double Net Metamaterials

Our DNM theory, presented in Sec. 2, reveals a significant finding concerning a spectrally isolated fundamental band that supports quasi-longitudinal EAW-like bulk modes. Unlike those found in single-network metamaterials or meta-atom-based systems, these modes possess a remarkable characteristic: the vanishing of their EM fields. This distinctive property leads us to observe a new type of BIC that naturally arises from the EAW-like behavior of the bulk modes within a vacuum slab configuration. Figures 2(b)–2(e) visually highlight this relationship between the EAW modes and the emergence of these BICs.

In the HDP picture, a standing wave slab solution exists at frequencies where the EAW solutions can be superposed such that the normal component of $\mathbf{j}_i$ vanishes at the slab boundaries. As the EAW fields are perpendicular to the vacuum plane waves, they perfectly decouple from radiative modes at the Γ-point of the surface Brillouin zone.[57] At the Γ-point, we thus obtain zero radiation and infinite lifetime [or Q-factor, here we define $Q = \frac{\Re(f)}{2\Im(f)}$] of the slab modes, which are therefore BICs in the center of the light cone. Note that the full nonapproximate scattering problem, while more complex and involving evanescent Floquet modes,[58] yields the same qualitative result, since the higher Bragg orders in the vacuum Rayleigh basis[59] are evanescent and nonradiative as the EAW band is below the first Wood anomaly; see Fig. 2(a).

To illustrate the above prediction in practice, we simulate a DNM slab with $\mathbf{P} = (0.4, 0.4, \frac{a}{2})$ and $N = 5$ unit cell thickness. The geometry is shown in Fig. 2(b). We apply Bloch-periodic boundary conditions in the x-y plane and scattering boundary conditions (numerical Sommerfeld conditions[60]) in the z direction and solve for the complex-valued frequencies (that is, we compute the quasi-normal slab modes). As predicted, multiple BICs with infinite lifetimes are located at the Γ-point and marked by red pentagrams in Fig. 2(c). The frequencies of

the BICs can be well approximated by the standing wave solution of the EAW with the predicted phase velocity of $\frac{1}{\sqrt{3}}c$ and hard wall boundary conditions ($\mathbf{j}_i = 0$). Since the EAW bulk band is spectrally isolated from the other nonevanescent bulk bands at low frequencies, the BICs are fundamentally prohibited from interfering with any non-BIC slab modes in the whole spectral range of the EAW band, in sharp contrast to BICs in photonic crystals.[3] At finite wave vectors away from the Γ-point, quasi-BICs are formed, since the EAW fields are not strictly orthogonal to the vacuum plane waves, which results in a weak coupling to the vacuum states. These quasi-BICs thus have a very large but finite Q-factor. The corresponding Q-factor values of the multiple quasi-BIC solutions near the Γ-point are shown in Figs. 2(c) and 2(d). The physics is reminiscent of a Fabry–Pérot resonator with mirrors that are perfectly reflective at normal incidence and are otherwise weakly transparent, but without using any mirrors. This physics yields a simple signature in scattering experiments: the transmittance resembles a Lorentzian line shape at a finite wave vector close to the BIC frequency. The center frequency forms a band that emanates from the BICs at the Γ-point and hyperbolically blueshifts with increasing wave vectors while the width of the Lorentzian gradually broadens. The simulated reflectance spectrum along the Γ-X direction is shown in Fig. 2(d) and agrees well with our theoretical modeling (see Note S4 and Figs. S6 and S7 in the Supplementary Material). The reflection spectrum, accounting for metal losses, is provided in Note S7 in the Supplementary Material.

The polarization of the quasi-BIC far-field is oriented in the direction of the wave vector, forming a "star" pattern in 2D momentum space, as shown in Fig. S9 in the Supplementary Material (see Note S5 in the Supplementary Material). This generates a singular point at the Γ-point where the BICs reside, where the polarization cannot be defined because the far-field vanishes. Around this point, the polarization pattern evidently exhibits a nontrivial topological winding number.[8] In our case, this topological vortex structure of the polarization field is a direct consequence of the quasi-longitudinal nature of the EAW modes. It is reminiscent of the electric field lines created by a point charge.

Finally, since the BICs originate from the standing wave solutions of the EAWs in the DNM slabs, the number of BIC modes and their frequency spacing are exclusively determined by the thickness of the DNM slab. A full theoretical model, assuming the HDP in a hard wall cavity, is given in Note S4 in the Supplementary Material. The theoretical model predicts the quasi-BIC bands, including their Q-factors (Fig. S7 in the Supplementary Material) and the transmission spectrum (Fig. S6 in the Supplementary Material). In particular, the model yields BIC modes that are equidistantly spaced at frequencies of $\frac{\omega a}{c} = l\frac{\kappa\pi}{N}$, where Na is the thickness of the DNM slab and $l \in \mathbb{N}$. The frequencies at which BIC modes occur on the Γ-point, and thus also the number of BIC modes that exist over the spectral range of the EAW band, are a function of the number of unit cells in the slab N (which can be a noninteger number). Extrapolating the linear dispersion relation of the HDP model to the Brillouin zone boundary, we expect $N-1$ BIC modes over the EAW band, which perfectly matches the full-wave simulation results of the $\mathbf{P} = (0.4, 0.4, \frac{a}{2})$ DNM in Fig. 2(e). Generally, the theoretical results agree with the simulations, even though the equidistant frequency spacing is perturbed in real DNMs.

4 Robustness to Symmetry-Breaking, Disorder, and Diffraction Orders

BICs residing at high symmetry points in the Brillouin zone in photonic crystal slabs and metasurfaces are typically protected by in-plane inversion (C_2) symmetry but can be disrupted by infinitesimal symmetry-breaking perturbations, as well as couplings to high diffraction orders.[26,27] Interestingly, despite being susceptible to symmetry breaking, the newly formed BICs in DNMs show exceptional robustness, retaining ultrahigh Q-factors. Our findings indicate that these new BICs persist even in the presence of symmetry breaking, disorder, and scattering into high diffraction orders. The exceptionally high robustness is linked to the HDP-effective medium nature of the DNMs.

To elucidate, we first demonstrate variations to the BICs imposed by local and periodic symmetry breaking. Two representative schemes were studied. (i) Deviations of the nets from their centrosymmetric positions [bottom left corner of Fig. 3(a)]. For example, a DNM with $\mathbf{P} = (0.4, 0.1, R)$ has only one in-plane mirror symmetry normal to the $[1\bar{1}0]$ direction, which is insufficient for creating symmetry-protected BICs.[8] (ii) Breaking the C_{4v} symmetry of a single net, while keeping the global mirror symmetry along $[1\bar{1}0]$, by adding thicker metallic cylinders between the nodes, as shown in the top-right corner of Fig. 3(a). In both cases, the Q-factor obeys an approximately inverse quadratic relationship $Q(\alpha) = Q_0\alpha^{-2}$ wherein α is the asymmetry parameter,[20] illustrated in Fig. 3(a). Q_0 is a constant determined by the specific network design.

Both cases possessing Q_0 higher than 2×10^4 were obtained, leading to high Q-factors even with considerable α-values. For example, $Q = 10^6$ for a relatively large $\alpha = 10^{-1}$. Note that the value of Q_0 alone, without consistently normalizing α, is arbitrary. However, if the perturbation is geometrical, α can be normalized by typical feature sizes (object dimension or unit cell size), while α is internally normalized if the perturbation is angular. The Q factor is typically higher than 10^6, even when structural changes occur at a scale comparable to the unit-cell size. This showcases the remarkable resilience of the novel BIC modes in DNMs. This excellent stability of the DNM-based BICs compared to previous findings[20] seems to stem from the macroscopic HDP effective medium nature of the DNMs. Microscopically, the surface current densities $\mathbf{J}$ on the metallic wires that are orthogonal to the propagation direction resemble an electrical quadruple that is symmetry-incompatible with free-space radiation. In the static limit, interactions between the currents on the two nets are negligible, so the total EM radiation vanishes irrespective of the networks' relative position, radii, etc. Finally, the symmetry-breaking schemes mentioned above, (i) and (ii), give rise to a linear radial vortex polarization around the Γ-point converting into linear polarization on the diagonal in wave-vector space, separating two regions with right- and left-turning elliptical polarization, respectively (Note S5 in the Supplementary Material). There is one spot on either side in wave-vector space where the polarization of the quasi-BICs is circularly polarized so that perfect circular dichroism in reflectance can be achieved with oblique angle of incidence at the circular polarization points at the quasi-BIC frequency.

Due to the successful application of the HDP model as an effective medium theory on DNMs and the fact that EAW modes are primarily determined by the morphology rather than

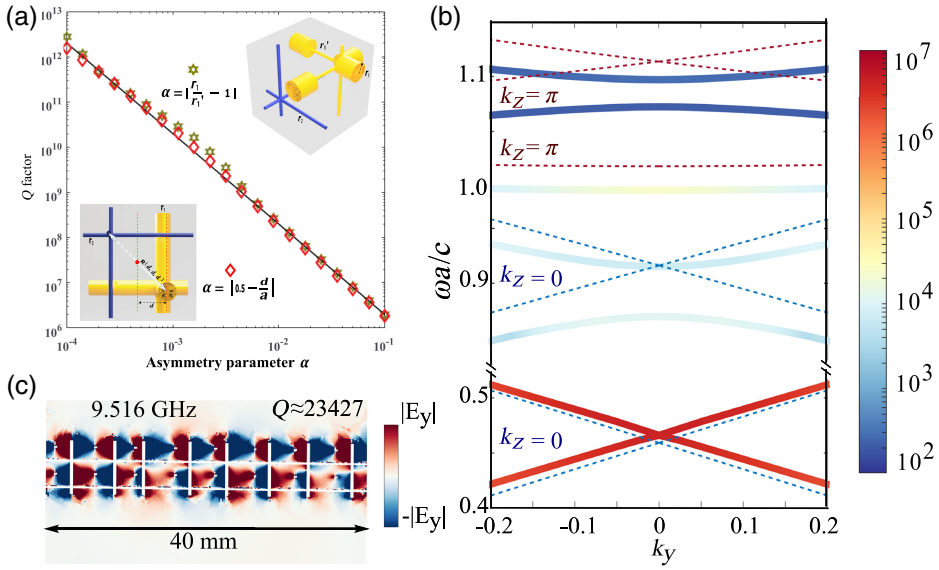

Fig. 3 (a) Q-factor as a function of the asymmetry parameter α. The two methods of symmetry breaking are illustrated in the upper-right corner (represented by green hexagonal stars) and the lower-left corner (represented by red diamonds). In both cases, the Q-factor closely follows an inverse quadratic power law $Q(\alpha) = Q_0\alpha^{-2}$ (solid line). (b) Band structure of DNM supercell slabs. Dashed lines correspond to an unperturbed DNM slab, back-folded into the supercell Brillouin zone, while the thick solid lines show the perturbed case. The line color encodes the Q-factor. The lower four bands with $k_z = 0$ correspond to back-folded modes originating from the in-plane EAW bands, initially outside the light cone. The upper three modes have $k_z = \pi$. The fifth band corresponds to the unperturbed BIC state at Γ, while the upper two bands are back-folded EAW standing waves. (c) Electric field distribution for the fifth band at Γ in the perturbed DNM supercell slab with $N = 2$ and 8 unit cells in the y direction with a random offset between the two nets. The ultrahigh Q-factor persists even though the supercell lattice constant allows coupling into the first diffraction order.

geometrical parameters, such as a and $\mathbf{P}$, it is reasonable to speculate that the new BICs are resilient to generic disorders. To illustrate this, we demonstrate high-Q states through numerical simulations, even when scattering into nonzero diffraction orders is possible. We specifically create a DNM slab with a large supercell of eight unit cells in the y direction, with a randomly generated inharmonious disorder in the spacing between the two nets while maintaining a fixed offset in the x and z directions of $\frac{a}{2}$. We fixed the thickness of this slab to $N = 2$. For the unperturbed DNMs, BICs appear at a frequency of 9.55 GHz at the Γ point, as shown in Fig. 2(e). A comparison of the band diagrams between the two structures is shown in Fig. 3(b). The perturbed supercell DNM slab retains the eigenmodes of the perfectly ordered DNM, weakly affecting their frequency position. The relative difference between the positions of the EAW standing waves at the Γ point is 0.05 GHz [see Fig. 3(b)]. Since the bands are back-folded into the Brillouin zone of the supercell geometry, we also fold back the bands of the unperturbed slab, shown as dashed lines. The Q-factors are represented by the color values of the solid lines for the perturbed case. The enlarged lattice plays a crucial role in allowing more diffraction channels, which permits the BIC around the frequency of 9.55 GHz, that is, $k_0 = 200\ \mathrm{m}^{-1}$ to radiate into the first Bragg order at $G \approx 160\ \mathrm{m}^{-1}$ for the supercell lattice constant of $8a = 40$ mm. In contrast, the unperturbed case is below the first Wood anomaly with the first Bragg order, $G = \frac{\pi}{a} \approx 1250\ \mathrm{m}^{-1}$. The enlarged supercell DNMs transform BICs into quasi-BICs, maintaining an extremely high Q-factor of 23,427 even above the Wood anomaly, where the first Bragg order in the y direction constitutes an additional radiation channel for which the longitudinal EAW-like modes are not perfectly decoupled from vacuum radiation. The electric field distribution corresponding to the supercell DNM slab with random variations in the y direction is depicted in Fig. 3(c). The fact that the field is tightly confined within the DNM slab confirms its weak coupling with the surrounding environment. More interestingly, since additional branches of the in-plane EAW wave are now back-folded in the continuum [see Fig. 3(c)], they also give rise to a quasi-BIC band with an even higher Q-factor of approximately 4×10^6 for the $k_z = 0$ band. This is because the back-folded modes inherit their main intensity from the unperturbed DNM, which lies in the first Bragg order of the supercell outside of the light cone ($G \approx 160\ \mathrm{m}^{-1}$) at the relevant frequencies ($k_0 \lessapprox 100\ \mathrm{m}^{-1}$).

In summary, the BICs discovered in DNMs exhibit remarkable stability and robustness, even in the presence of extreme symmetry breaking and disorder above the Wood anomaly, which can be attributed to the HDP's effective-medium nature of DNMs. Consequently, these new BIC modes in DNMs hold immense potential for various optical applications, including optoelectronic devices, integrated photonic circuits, and waveguide-based devices. By leveraging their exceptional stability

and robustness, DNMs can pave the way for developing next-generation ultracompact and highly efficient optical systems.

5 Quasi-BICs with Ultrahigh *Q* Factors and Subwavelength Dimension

Benefiting from the peculiar non-Maxwellian HDP effective medium nature of the DNMs with approximately vanishing overall EM fields, they might be used to build ultrahigh-Q individual quasi-BIC resonators with subwavelength dimensions. To elaborate on this potential, we study quasi-BIC resonances in a cubic DNM microresonator [Fig. 4(a)]. In the HDP effective medium picture, the eigenmodes in the individual cubic structure obey the 3D hard-boundary condition; that is, the normal current component of both plasmas must vanish at the cubic boundaries. This leads to eigenfrequencies $\omega_{mnl} = \frac{v_g \pi}{L}|\mathbf{n}|$ with $\mathbf{n} = (m, n, l) \in \mathbb{N}^3$. The (m, n, l) indices label the allowed Cartesian momentum components in the cubic cavity responsible for the resonances. The lowest three resonance frequencies involve momentums marked as colored spheres in Fig. 4(b). The lowest mode is threefold degenerate ($|\mathbf{n}|^2 = 1$, red spheres, T_{1u} irreducible representation in the O_h group[48]). The second mode is also threefold degenerate ($|\mathbf{n}|^2 = 2$, blue spheres, T_{2g} irrep), while the third mode is nondegenerate ($|\mathbf{n}|^2 = 3$, yellow spheres, A_{2u} irrep). Increasing the box length, L, simply redshifts the modes, as shown in Fig. 4(c) (dashed lines). For the DNMs, similar behavior is expected because of the HDP effective medium approximation. By increasing the DNM cube edge length, L, from 10 to 20 mm (two unit cells to four unit cells along the Cartesian axes), we find approximately the same trend in the frequency shifts, as in the HDP model. On the other hand, the DNM cavities exhibit a finite lifetime. The frequencies of the lowest three modes of the DNM cubic resonator are displayed in Fig. 4(c) as solid-hued lines, whose color represents the Q-factors. Note that we chose the resonator geometry such that the inversion center of the double net is in the center. This implies that individual nets are cut along their long axis at the boundary of the resonator at 15 mm. We avoid such cuttings, explaining the discontinuity of the solid lines in Fig. 4(c). The graph confirms the validity of the effective medium description of the DNMs. It becomes, however, clear that the microscopic boundary configuration plays a crucial role in determining the Q-factor, which ranges from 10^2 to 10^7. Similar to the slab configuration, the quasi-BIC states manifest themselves as resonances in the scattering cross sections (SCs). Figure 4(d) shows a slightly asymmetric Fano resonance dip in the SC at the fundamental quasi-BIC mode at 7.54 GHz, whose Q-factor is as high as 2400 for the cube's edge length of 12.5 mm.

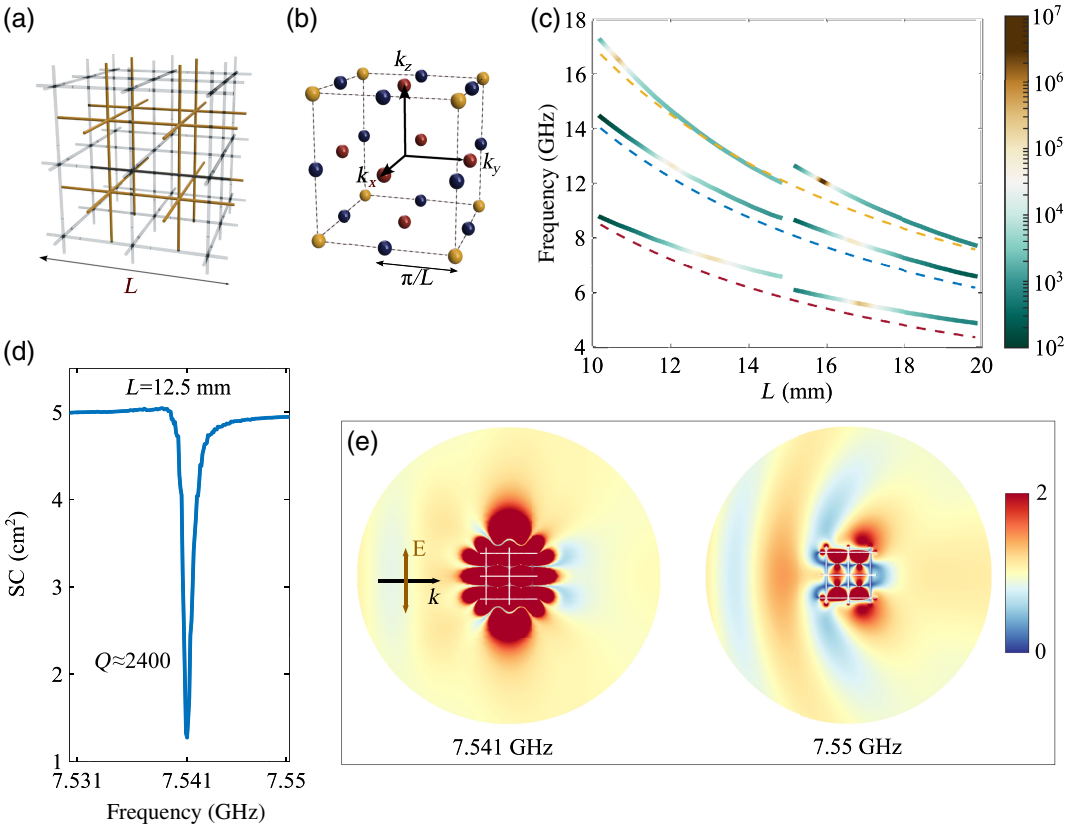

Fig. 4 (a) Schematic diagram of a DNM microcavity of length L. (b) The fundamental modes are formed by EAW standing waves and are characterized by discrete reciprocal vectors marked through red, blue, and yellow balls. (c) The three fundamental mode frequencies as a function of L. The dashed lines are the HDP predictions, and the solid thick lines are the simulated DNM resonator states. The color encodes the Q-factor. (d) SC as a function of frequency for an $L = 12.5$ mm DNM resonator. (e) Electric field distribution in the DNM microcavity at the resonance frequency (left) and away from the resonance (right).

The appearance of an SC dip rather than a peak is owed to the destructive interference with the background scatterings, whose asymmetry is more pronounced for lower Q-factor resonances. The fundamental quasi-BICs mode is located in frequency space at approximately the boundary between the Rayleigh scattering and the Mie scattering regimes without high-index dielectric filling within the structure. It is, however, possible to drive the quasi-BICs to operate within the Rayleigh scattering regime by introducing high-index dielectrics. The total field intensity in Fig. 4(e) shows the reduced disturbance to the incident plane wave and the pronounced field build-up in the DNMs on the resonator frequency at 7.541 GHz, when compared to the off-resonance frequency at 7.55 GHz.

The extremely small physical size of the resonator (on the order of a few unit cells) is in stark contrast to previously reported purely dielectric quasi-BIC resonators. The reduced SC and thus perturbation to the incident EM field and the gigantic field build-up in the DNM cube could give rise to stealth and highly sensitive microwave probing antenna opportunities.

6 Conclusions

In summary, this study presents an approach to achieving photonic BICs in DNMs. The HDP is employed as an effective medium model for DNMs. An exact analytical solution for the refractive index of EAWs is derived in the long wavelength limit. The non-Maxwellian HDP leads to a unique type of quasi-longitudinal EAW band, which results in the emergence of BICs at arbitrary frequencies within the frequency regime of the EAW wave, free of non-BIC resonances and shows remarkable stability and robustness even in the presence of strong geometrical perturbations, symmetry breaking, general disorder, and being above the Wood anomaly, where coupling into higher Bragg orders is possible. Importantly, the BIC modes can maintain high Q-factors even if the structure is contained within a subwavelength scale, as demonstrated for an ultrasmall cubic DNM resonator. The discovery of these resilient BIC modes in DNMs presents exciting opportunities for various optical applications, including optoelectronic devices, integrated photonic circuits, and waveguide-based devices. It also holds the potential for developing innovative ultracompact and highly efficient optical systems. This study provides valuable insights into optical metamaterials and their practical applications. While the theoretical predictions, based on a lossless plasma and a corresponding perfectly conducting double net, can be readily explored in the microwave regime, an extension of the theory in future work would be desirable to quantify the nonradiative contribution to the quasi-BIC lifetimes at infrared frequencies.

Data, Materials, and Code Availability

Data underlying the results presented in this paper may be obtained from the authors upon reasonable request.

Acknowledgments

We acknowledge funding from the Swiss National Science Foundation (Grant No. 188647) and from the Adolphe Merkle Foundation. W.H. Wang also expresses gratitude to her newborn daughter, DiangDiang, for inspiring and stimulating the discussion. The authors have no relevant financial interests regarding the paper and no other potential conflicts of interest to disclose.

References

1. J. von Neumann and E. P. Wigner, "Uber merkwürdige diskrete Eigenwerte. über das Verhalten von Eigenwerten bei adiabatischen Prozessen," *Phys. Z.* **30**, 467–470 (1929).
2. F. H. Stillinger and D. R. Herrick, "Bound states in the continuum," *Phys. Rev. A* **11**, 446–454 (1975).
3. C. W. Hsu et al., "Bound states in the continuum," *Nat. Rev. Mater.* **5**(9), 16048 (2016).
4. D. Marinica, A. Borisov, and S. Shabanov, "Bound states in the continuum in photonics," *Phys. Rev. Lett.* **100**(18), 183902 (2008).
5. C. W. Hsu et al., "Observation of trapped light within the radiation continuum," *Nature* **499**(7457), 188–191 (2013).
6. M. I. Molina, A. E. Miroshnichenko, and Y. S. Kivshar, "Surface bound states in the continuum," *Phys. Rev. Lett.* **108**(7), 070401 (2012).
7. W. Chen, Y. Chen, and W. Liu, "Singularities and Poincaré indices of electromagnetic multipoles," *Phys. Rev. Lett.* **122**(15), 153907 (2019).
8. B. Zhen et al., "Topological nature of optical bound states in the continuum," *Phys. Rev. Lett.* **113**(25), 257401 (2014).
9. H. M. Doeleman et al., "Experimental observation of a polarization vortex at an optical bound state in the continuum," *Nat. Photonics* **12**(7), 397–401 (2018).
10. Y. Guo, M. Xiao, and S. Fan, "Topologically protected complete polarization conversion," *Phys. Rev. Lett.* **119**(16), 167401 (2017).
11. Y. Yang et al., "Analytical perspective for bound states in the continuum in photonic crystal slabs," *Phys. Rev. Lett.* **113**(3), 037401 (2014).
12. A. Lyapina et al., "Bound states in the continuum in open acoustic resonators," *J. Fluid Mech.* **780**, 370–387 (2015).
13. Z. Yu et al., "High-dimensional communication on etchless lithium niobate platform with photonic bound states in the continuum," *Nat. Commun.* **11**(1), 2602 (2020).
14. Y. Chen et al., "Observation of intrinsic chiral bound states in the continuum," *Nature* **613**(7944), 474–478 (2023).
15. S. I. Azzam and A. V. Kildishev, "Photonic bound states in the continuum: from basics to applications," *Adv. Opt. Mater.* **9**(1), 2001469 (2021).
16. S. Romano et al., "Optical biosensors based on photonic crystals supporting bound states in the continuum," *Materials* **11**(4), 526 (2018).
17. C. Huang et al., "Ultrafast control of vortex microlasers," *Science* **367**(6481), 1018–1021 (2020).
18. B. Wang et al., "Generating optical vortex beams by momentum-space polarization vortices centred at bound states in the continuum," *Nat. Photonics* **14**(10), 623–628 (2020).
19. A. Kodigala et al., "Lasing action from photonic bound states in continuum," *Nature* **541**(7636), 196–199 (2017).
20. K. Koshelev et al., "Asymmetric metasurfaces with high-Q resonances governed by bound states in the continuum," *Phys. Rev. Lett.* **121**(19), 193903 (2018).
21. M. V. Rybin et al., "High-Q supercavity modes in subwavelength dielectric resonators," *Phys. Rev. Lett.* **119**, 243901 (2017).
22. S. T. Ha et al., "Directional lasing in resonant semiconductor nanoantenna arrays," *Nat. Nanotech.* **13**(11), 1042–1047 (2018).
23. L. Fonda and R. G. Newton, "Theory of resonance reactions," *Ann. Phys.* **10**(4), 490–515 (1960).
24. H. Friedrich and D. Wintgen, "Physical realization of bound states in the continuum," *Phys. Rev. A* **31**(6), 3964–3966 (1985).
25. V. A. Sablikov and A. A. Sukhanov, "Helical bound states in the continuum of the edge states in two dimensional topological insulators," *Phys. Lett. A* **379**(30–31), 1775–1779 (2015).
26. W. Liu et al., "Circularly polarized states spawning from bound states in the continuum," *Phys. Rev. Lett.* **123**(11), 116104 (2019).
27. T. Yoda and M. Notomi, "Generation and annihilation of topologically protected bound states in the continuum and circularly

polarized states by symmetry breaking," *Phys. Rev. Lett.* **125**(5), 053902 (2020).
28. Z. F. Sadrieva et al., "Transition from optical bound states in the continuum to leaky resonances: role of substrate and roughness," *ACS Photonics* **4**(4), 723–727 (2017).
29. N. Engheta and R. W. Ziolkowski, *Metamaterials: Physics and Engineering Explorations*, John Wiley, New York (2006).
30. D. R. Smith, J. B. Pendry, and M. C. K. Wiltshire, "Metamaterials and negative refractive index," *Science* **305**(5685), 788–792 (2004).
31. J. Pendry, "A chiral route to negative refraction," *Science* **306**(5700), 1353–1355 (2004).
32. I. Liberal and N. Engheta, "Near-zero refractive index photonics," *Nat. Photonics* **11**(3), 149–158 (2017).
33. A. M. Mahmoud and N. Engheta, "Wave-matter interactions in epsilon-and-mu-near-zero structures," *Nat. Commun.* **5**(1), 5638 (2014).
34. S. S. Oh and O. Hess, "Chiral metamaterials: enhancement and control of optical activity and circular dichroism," *Nano Converg.* **2**(1), 24 (2015).
35. E. S. A. Goerlitzer et al., "The beginner's guide to chiral plasmonics: mostly harmless theory and the design of large-area substrates," *Adv. Opt. Mater.* **9**, 2100378 (2021).
36. C. Kilchoer et al., "Strong circular dichroism in single gyroid optical metamaterials," *Adv. Opt. Mater.* **8**(13), 1902131 (2020).
37. A. Demetriadou and J. B. Pendry, "Taming spatial dispersion in wire metamaterial," *J. Phys. Condens. Matter* **20**(29), 295222 (2008).
38. S. I. Maslovski and M. G. Silveirinha, "Nonlocal permittivity from a quasistatic model for a class of wire media," *Phys. Rev. B* **80**, 245101 (2009).
39. J. A. Dolan et al., "Optical properties of gyroid structured materials: from photonic crystals to metamaterials," *Adv. Opt. Mater.* **3**(1), 12–32 (2015).
40. A. Alvarez-Fernandez et al., "Block copolymer directed metamaterials and metasurfaces for novel optical devices," *Adv. Opt. Mater.* **9**, 2100175 (2021).
41. W.-J. Chen et al., "Metamaterials with index ellipsoids at arbitrary k-points," *Nat. Commun.* **9**(1), 2086 (2018).
42. H. Latioui and M. G. Silveirinha, "Light tunneling anomaly in interlaced metallic wire meshes," *Phys. Rev. B* **96**(19), 195132 (2017).
43. D. Sakhno, E. Koreshin, and P. A. Belov, "Longitudinal electromagnetic waves with extremely short wavelength," *Phys. Rev. B* **104**(10), L100304 (2021).
44. K. Hur et al., "Three-dimensionally isotropic negative refractive index materials from block copolymer self-assembled chiral gyroid networks," *Angew. Chem. Int. Ed.* **50**(50), 11985–11989 (2011).
45. A. W. Powell et al., "Dark mode excitation in three-dimensional interlaced metallic meshes," *ACS Photonics* **8**(3), 841–846 (2021).
46. W. Wang et al., "Photonic topological fermi nodal disk in non-Hermitian magnetic plasma," *Light Sci. Appl.* **9**(1), 40 (2020).
47. W. Gao et al., "Photonic Weyl degeneracies in magnetized plasma," *Nat. Commun.* **7**(1), 12435 (2016).
48. M. S. Dresselhaus, *Group Theory : Application to the Physics of Condensed Matter*, Springer-Verlag, Berlin (2008).
49. S. P. Gary and R. L. Tokar, "Electron-acoustic mode," *Phys. Fluids* **28**(8), 2439–2441 (1985).
50. D. S. Montgomery et al., "Observation of stimulated electron-acoustic-wave scattering," *Phys. Rev. Lett.* **87**(15), 155001 (2001).
51. M. A. Hellberg et al., "Electron-acoustic waves in the laboratory: an experiment revisited," *J. Plasma Phys.* **64**(4), 433–443 (2000).
52. S. Singh and G. Lakhina, "Generation of electron-acoustic waves in the magnetosphere," *Planet. Space Sci.* **49**(1), 107–114 (2001).
53. J. B. Pendry et al., "Low frequency plasmons in thin-wire structures," *J. Phys. Condens. Matter* **10**(22), 4785–4809 (1998).
54. M. G. Silveirinha and C. A. Fernandes, "Homogenization of 3-D-connected and nonconnected wire metamaterials," *IEEE Trans. Microwave Theory Tech.* **53**(4), 1418–1430 (2005).
55. J. Shin, J.-T. Shen, and S. Fan, "Three-dimensional electromagnetic metamaterials that homogenize to uniform non-Maxwellian media," *Phys. Rev. B* **76**(11), 113101 (2007).
56. S. Lannebere, T. A. Morgado, and M. G. Silveirinha, "First principles homogenization of periodic metamaterials and application to wire media," *C.R. Phys.* **21**(4–5), 367–388 (2020).
57. J. Joannopoulos et al., *Photonic Crystals: Molding the Flow of Light*, 2nd ed., Princeton University Press, Princeton (2011).
58. M. Saba and G. E. Schroder-Turk, "Bloch modes and evanescent modes of photonic crystals: weak form solutions based on accurate interface triangulation," *Crystals* **5**(1), 14–44 (2015).
59. L. Rayleigh, "On the dynamical theory of gratings," *Proc. R. Soc. Lond. A* **79**(532), 399–416 (1907).
60. A. Sommerfeld, *Partial Differential Equations in Physics*, Academic Press, New York (1949).
61. R. Fitzpatrick, *Plasma Physics: An Introduction*, CRC Press, Taylor & Francis Group, Boca Raton, Florida (2015).
62. D. Jin et al., "Topological magnetoplasmon," *Nat. Commun.* **7**(1), 13486 (2016).
63. S. I. Maslovski, S. A. Tretyakov, and P. A. Belov, "Wire media with negative effective permittivity: a quasi-static model," *Microwave Opt. Technol. Lett.* **35**(1), 47–51 (2002).
64. O. Delgado-Friedrichs and M. O'Keeffe, "Reticular chemistry structure resource," http://rcsr.anu.edu.au (accessed 11 May, 2021).
65. S. G. Markande et al., "A chiral family of triply-periodic minimal surfaces derived from the quartz network," arXiv:1805.07034 (2018).
66. W. Setyawan and S. Curtarolo, "High-throughput electronic band structure calculations: challenges and tools," *Comput. Mater. Sci.* **49**(2), 299–312 (2010).
67. T. Bradley, C. Bradley, and A. Cracknell, *The Mathematical Theory of Symmetry in Solids: Representation Theory for Point Groups and Space Groups*, Clarendon Press, Oxford (1972).
68. M. I. Aroyo, Ed., *International Tables for Crystallography A: Space-group Symmetry*, 2nd ed., vol. **A**, International Union of Crystallography, Chester, England (2016).
69. M. Saba et al., "Group theory of circular-polarization effects in chiral photonic crystals with four-fold rotation axes applied to the eight-fold intergrowth of gyroid nets," *Phys. Rev. B* **88**(24), 245116 (2013).

Wenhui Wang achieved her PhD from the University of Science and Technology of China, in 2016. Afterward, she became a member of the Meta Materials Group at Birmingham University, United Kingdom, and subsequently joined the Research Laboratory for Quantum Materials at Singapore University of Technology and Design. The research presented here was conducted during her time as a senior researcher within the Soft Matter Physics Group at the Adolphe Merkle Institute in Switzerland. Her research interests span metamaterials, plasma dynamics, and topological photonics.

Matthias Saba received a PhD in physics in 2015 from the University of Erlangen–Nuremberg (Germany). He subsequently joined the Condensed Matter Theory Group at Imperial College London, where he studied 3D topological photonic materials and metamaterials. His current research interests as a group leader in the Soft Matter Physics Group at the Adolphe Merkle Institute (Switzerland) include double-net metamaterials, chiral thermal plasmonic crystals, and the theory of photonic states in finite periodic and disordered structures.

Biographies of the other authors are not available.